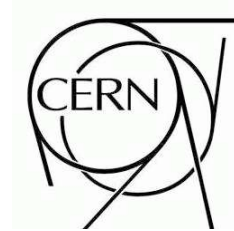


ATLAS NOTE

ATL-PHYS-PUB-2009-002

April 24, 2009



The Expected Performance of the Inner Detector.

The ATLAS Collaboration¹⁾

This note is part of CERN-OPEN-2008-020. This version of the note should not be cited: all citations should be to CERN-OPEN-2008-020.

Abstract

The ATLAS inner detector will see of the order of 1000 charged particle tracks for every beam crossing at the design luminosity of the CERN Large Hadron Collider (LHC). This paper summarizes the design of the detector and outlines the reconstruction software. The expected performance for reconstructing single particles is presented, along with an indication of the vertexing capabilities. The effect of the detector material on electrons and photons is discussed along with methods for improving their reconstruction. The studies presented focus on the performance expected for the initial running at the start-up of the LHC.

¹⁾This note prepared by A. Andreazza, J.R. Batley, W. Bell, E. Bouhova-Thacker, T. Cornelissen, M. Donega, M. Elsing, D. Froidevaux, I. Gavrilenko, G. Gorfine, S.J. Haywood, R. Henderson, V. Kartvelishvili, T. Koffas, V. Kostyukhin, J. Lee, M. Leyton, W. Liebig, A.K. Morley, E. Moyse, G. Piacquadio, T. Petersen, A. Poppleton, D. Price, K. Prokofiev, C. Ruwiedel, A. Salzburger, C. Schmitt, M. Siebel, L. Vacavant, J.-B. de Vivie de Regie, C.P. Ward, A. Wildauer, H. Zhu.



1 Introduction

In ATLAS, at the LHC design luminosity of $10^{34} \text{ cm}^{-2}\text{s}^{-1}$, approximately 1000 particles will emerge from the collision point every 25 ns within $|\eta| < 2.5$, creating a very large track density in the detector. To achieve the momentum and vertex resolution requirements imposed by the benchmark physics processes, high-precision measurements will be made in the inner detector (ID), shown in Fig. 1. Pixel and silicon microstrip (SCT) trackers, used in conjunction with the straw tubes of the transition radiation tracker (TRT), will make high-granularity measurements. The original performance specifications were set out in 1994 and are detailed in [1] – the focus being on challenging physics channels such as the measurement of leptons from the decays of heavy gauge bosons and the tagging of b -quark jets.

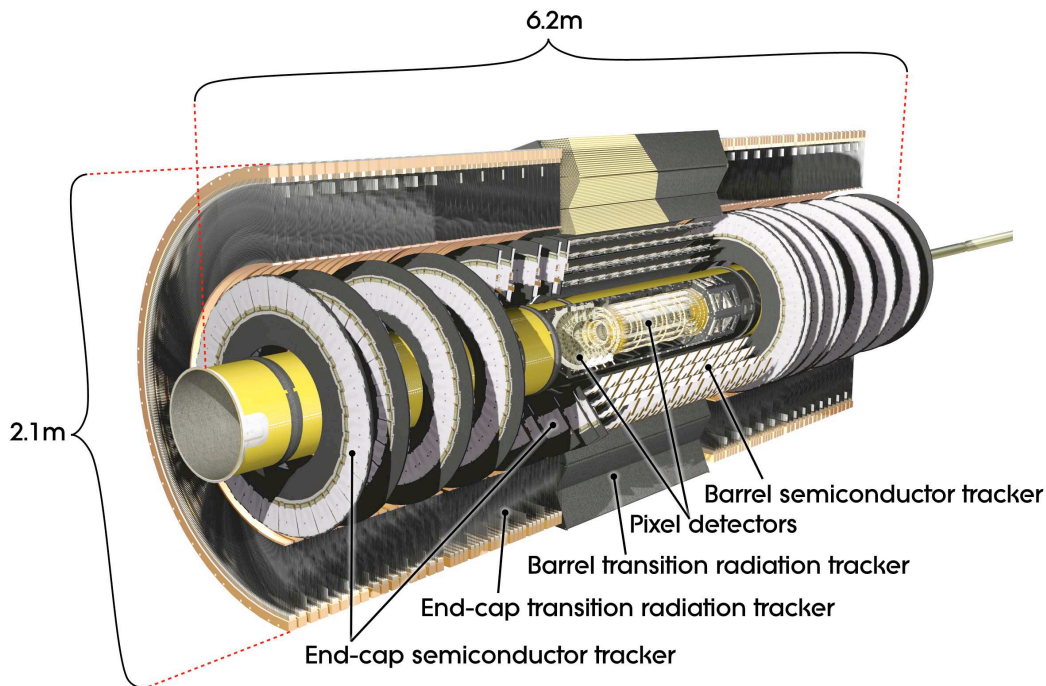


Figure 1: Cut-away view of the ATLAS inner detector.

The ID surrounds the LHC beam-pipe which is inside a radius of 36 mm. The layout of the detector is illustrated in Fig. 2 and detailed in [2]. Its basic parameters are summarised in Table 1. The ID is immersed in a 2 T magnetic field generated by the central solenoid, which extends over a length of 5.3 m with a diameter of 2.5 m.

The precision tracking detectors (pixels and SCT) cover the region $|\eta| < 2.5$. In the barrel region, they are arranged on concentric cylinders around the beam axis while in the end-cap regions, they are located on disks perpendicular to the beam axis. The highest granularity is achieved around the vertex region using silicon pixel sensors. All pixel modules are identical and the minimum pixel size on a sensor is $50 \times 400 \text{ } \mu\text{m}^2$. The pixel layers are segmented in $R - \phi$ and z with typically three pixel layers crossed by each track. The first layer, called the “vertexing layer”, is at a radius of 51 mm. The intrinsic accuracies in the barrel are 10 μm ($R - \phi$) and 115 μm (z) and in the disks are 10 μm ($R - \phi$) and 115 μm (R). The pixel detector has approximately 80.4 million readout channels.

For the SCT, eight strip layers (four space points) are crossed by each track. In the barrel region, this detector uses small-angle (40 mrad) stereo strips to measure both coordinates, with one set of strips in each layer parallel to the beam direction, measuring $R - \phi$. Each side of a detector module consists of

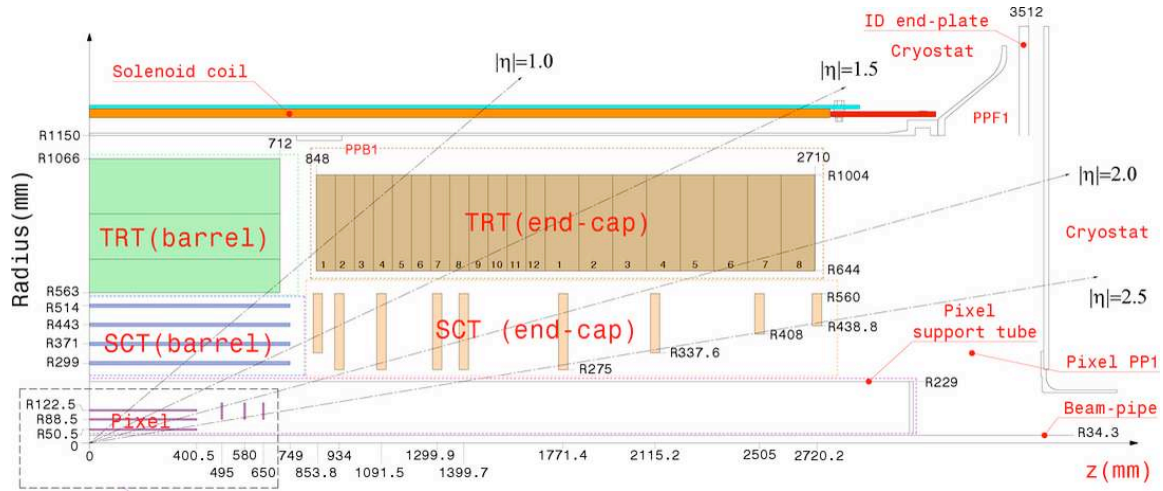


Figure 2: Plan view of a quarter-section of the ATLAS inner detector showing each of the major elements with its active dimensions.

Item		Radial extension (mm)	Length (mm)
Pixel	Overall envelope	$45.5 < R < 242$	$0 < z < 3092$
3 cylindrical layers	Sensitive barrel	$50.5 < R < 122.5$	$0 < z < 400.5$
2 × 3 disks	Sensitive end-cap	$88.8 < R < 149.6$	$495 < z < 650$
SCT	Overall envelope	$255 < R < 549$ (barrel)	$0 < z < 805$
		$251 < R < 610$ (end-cap)	$810 < z < 2797$
4 cylindrical layers	Sensitive barrel	$299 < R < 514$	$0 < z < 749$
2 × 9 disks	Sensitive end-cap	$275 < R < 560$	$839 < z < 2735$
TRT	Overall envelope	$554 < R < 1082$ (barrel)	$0 < z < 780$
		$617 < R < 1106$ (end-cap)	$827 < z < 2744$
73 straw planes	Sensitive barrel	$563 < R < 1066$	$0 < z < 712$
160 straw planes	Sensitive end-cap	$644 < R < 1004$	$848 < z < 2710$

Table 1: Main parameters of the inner detector.

two 6.4 cm long, daisy-chained sensors with a strip pitch of 80 μm . In the end-cap region, the detectors have a set of strips running radially and a set of stereo strips at an angle of 40 mrad. The mean pitch of the strips is also approximately 80 μm . The intrinsic accuracies per module in the barrel are 17 μm ($R-\phi$) and 580 μm (z) and in the disks are 17 μm ($R-\phi$) and 580 μm (R). The total number of readout channels in the SCT is approximately 6.3 million.

A large number of hits (typically 30 per track, with a maximum of 36, see Fig. 34) is provided by the 4 mm diameter straw tubes of the TRT, which enables track-following up to $|\eta| = 2.0$. The TRT only provides $R-\phi$ information, for which it has an intrinsic accuracy of 130 μm per straw. In the barrel region, the straws are parallel to the beam axis and are 144 cm long, with their wires divided into two halves, approximately at $\eta = 0$. In the end-cap region, the 37 cm long straws are arranged radially in wheels. The total number of TRT readout channels is approximately 351,000.

Item	Intrinsic accuracy (μm)	Alignment tolerances (μm)		
		Radial (R)	Axial (z)	Azimuth ($R-\phi$)
Pixel				
Layer-0	10 ($R-\phi$) 115 (z)	10	20	7
Layer-1 and -2	10 ($R-\phi$) 115 (z)	20	20	7
Disks	10 ($R-\phi$) 115 (R)	20	100	7
SCT				
Barrel	17 ($R-\phi$) 580 (z) ¹	100	50	12
Disks	17 ($R-\phi$) 580 (R) ¹	50	200	12
TRT	130			30 ²

1. Arises from the 40 mrad stereo angle between back-to-back sensors on the SCT modules with axial (barrel) or radial (end-cap) alignment of one side of the structure. The result is pitch-dependent for end-cap SCT modules.
2. The quoted alignment accuracy is related to the TRT drift-time accuracy.

Table 2: Intrinsic measurement accuracies and mechanical alignment tolerances for the inner detector sub-systems, as defined by the performance requirements of the ATLAS experiment. The numbers in the table correspond to the single-module accuracy for the pixels, to the effective single-module accuracy for the SCT and to the drift-time accuracy of a single straw for the TRT.

The combination of precision trackers at small radii with the TRT at a larger radius gives very robust pattern recognition and high precision in both $R-\phi$ and z coordinates. The straw hits at the outer radius contribute significantly to the momentum measurement, since the lower precision per point compared to the silicon is compensated by the large number of measurements and longer measured track length.

The inner detector system provides tracking measurements in a range matched by the precision measurements of the electromagnetic calorimeter [2]. The electron identification capabilities are enhanced by the detection of transition-radiation photons in the xenon-based gas mixture of the straw tubes. The semiconductor trackers also allow impact parameter measurements and vertex reconstruction (“vertexing”) for heavy-flavour and τ -lepton tagging. The secondary vertex measurement performance is enhanced by the innermost layer of pixels, at a radius of about 5 cm.

Charged particle tracks with transverse momentum $p_T > 0.5 \text{ GeV}$ and $|\eta| < 2.5$ are reconstructed and measured in the inner detector and the solenoid field. However, the efficiency at low momentum is limited because of the large material effect in the inner detector (see Fig. 3). The intrinsic measurement performance expected for each of the inner detector sub-systems is summarised in Table 2. This performance has been studied extensively over the years [1], both before and after irradiation of production modules, and also, more recently, during the combined test beam (CTB) runs in 2004 [2,3] and in a series

of cosmic-ray tests in 2006 [2, 4]. The results have been used to update and validate the modelling of the detector response in the Monte-Carlo simulation. This paper describes the expected performance of the inner detector in terms of tracking, vertexing and particle identification. The alignment of the inner detector is described elsewhere ([2] and the references therein).

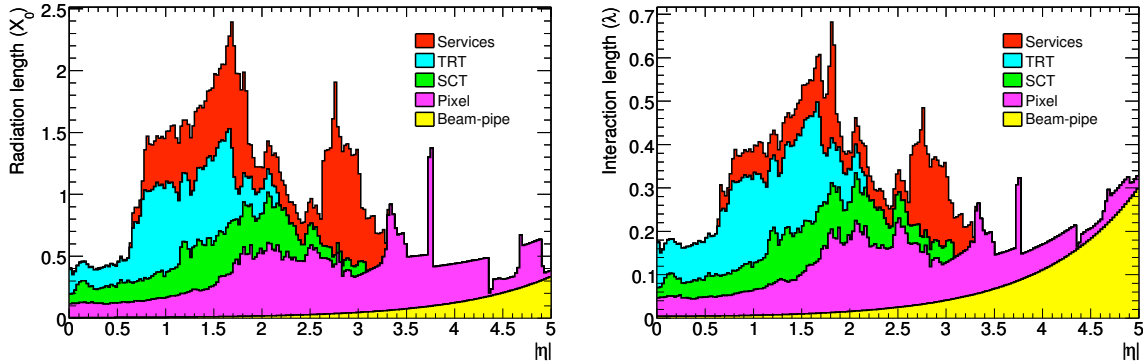


Figure 3: Material distribution (X_0 , λ) at the exit of the ID envelope, including the services and thermal enclosures. The distribution is shown as a function of $|\eta|$ and averaged over ϕ . The breakdown indicates the contributions of external services and of individual sub-detectors, including services in their active volume.

2 Track reconstruction

The inner detector track reconstruction software [5] follows a modular and flexible software design, which includes features covering the requirements of both the inner detector and muon spectrometer [2] reconstruction. These features comprise a common event data model [6] and detector description [7], which allow for standardised interfaces to all reconstruction tools, such as track extrapolation, track fitting including material corrections and vertex fitting. The extrapolation package combines propagation tools with an accurate and optimised description of the active and passive material of the full detector [8] to allow for material corrections in the reconstruction process. The suite of track-fitting tools includes global- χ^2 and Kalman-filter techniques, and also more specialised fitters such as dynamic noise adjustment (DNA) [9], Gaussian-sum filters (GSF) [10] and deterministic annealing filters [11]. Optimisation of these tools continues and their performance will need to be evaluated on real data. The tools intended to cope with electron bremsstrahlung (DNA and GSF – see Section 5.1) will be run after the track reconstruction, as part of the electron-photon identification. Other common tracking tools are provided, including those to apply calibration corrections at later stages of the pattern recognition, to correct for module deformations or to resolve hit-association ambiguities.

Track reconstruction in the inner detector is logically sub-divided into three stages:

1. A pre-processing stage, in which the raw data from the pixel and SCT detectors are converted into clusters and the TRT raw timing information is translated into calibrated drift circles. The SCT clusters are transformed into space-points, using a combination of the cluster information from opposite sides of a SCT module.
2. A track-finding stage, in which different tracking strategies [5, 12], optimised to cover different applications, are implemented. (The results of studies of the various algorithms are reported elsewhere [13].) The default tracking exploits the high granularity of the pixel and SCT detectors to

find prompt tracks originating from the vicinity of the interaction region. First, track seeds are formed from a combination of space-points in the three pixel layers and the first SCT layer. These seeds are then extended throughout the SCT to form track candidates. Next, these candidates are fitted, “outlier” clusters are removed, ambiguities in the cluster-to-track association are resolved, and fake tracks are rejected. This is achieved by applying quality cuts. For example, a cut is made on the number of associated clusters, with explicit limits set on the number of clusters shared between several tracks and the number of holes per track (a hole is defined as a silicon sensor crossed by a track without generating any associated cluster). The selected tracks are then extended into the TRT to associate drift-circle information in a road around the extrapolation and to resolve the left-right ambiguities. Finally, the extended tracks are refitted with the full information of all three detectors. The quality of the refitted tracks is compared to the silicon-only track candidates and hits on track extensions resulting in bad fits are labelled as outliers (they are kept as part of the track but are not included in the fit).

A complementary track-finding strategy, called back-tracking, searches for unused track segments in the TRT. Such segments are extended into the SCT and pixel detectors to improve the tracking efficiency for secondary tracks from conversions or decays of long-lived particles.

3. A post-processing stage, in which a dedicated vertex finder is used to reconstruct primary vertices. This is followed by algorithms dedicated to the reconstruction of photon conversions and of secondary vertices.

3 Tracking performance

3.1 Introduction to performance studies

The expected performance of the tracking system for reconstructing single particles and particles in jets is determined using a precise modelling of the individual detector response (including electronic noise and inefficiencies), geometry and passive material in the simulation. In this paper, a consistent set of selection cuts for reconstructed tracks has been used. Generally, only prompt particles (those originating from the primary vertex) with $p_T > 1$ GeV and $|\eta| < 2.5$ are considered. Standard quality cuts require reconstructed tracks to have at least seven precision hits (pixels and SCT). In addition, the transverse and longitudinal impact parameters at the perigee must fulfil respectively $|d_0| < 2$ mm and $|z_0 - z_v| \times \sin \theta < 10$ mm, where z_v is the position of the primary vertex along the beam and θ is the polar angle of the track. Stricter selection cuts, called *b*-tagging cuts, are defined by: at least two hits in the pixels, one of which should be in the vertexing layer, as well as $|d_0| < 1$ mm and $|z_0 - z_v| \times \sin \theta < 1.5$ mm. A reconstructed track is matched to a Monte-Carlo particle if at least 80% of its hits were created by that particle. The efficiency is defined as the fraction of particles which are matched to reconstructed tracks passing the quality cuts, and the fake rate is defined as the fraction of reconstructed tracks passing the quality cuts which are not matched to a particle.

3.2 Track parameter resolutions

The resolution of a track parameter X can be expressed as a function of p_T as:

$$\sigma_X(p_T) = \sigma_X(\infty)(1 \oplus p_X/p_T) \quad (1)$$

where $\sigma_X(\infty)$ is the asymptotic resolution expected at infinite momentum, p_X is a constant representing the value of p_T for which the intrinsic and multiple-scattering terms in the equation are equal for the parameter X under consideration and \oplus denotes addition in quadrature. This expression is approximate,

working well at high p_T (where the resolution is dominated by the intrinsic detector resolution) and at low p_T (where the resolution is dominated by multiple scattering). $\sigma_X(\infty)$ and p_X are implicitly functions of the pseudorapidity. Figures 4, 5 and 6 show the momentum resolution for isolated muons and the transverse and longitudinal impact parameter resolutions for isolated pions²⁾, all without a beam constraint and assuming the effects of misalignment, miscalibration and pile-up to be negligible. The resolutions are taken as the RMS evaluated over a range which includes 99.7% of the data (corresponding to $\pm 3\sigma$ for a Gaussian distribution). The TRT measurements are included in the track fits for tracks with $|\eta| < 2.0$, beyond which there are no further TRT measurements. Table 3 shows the values of $\sigma_X(\infty)$ and p_X for tracks in two η -regions, corresponding to the barrel and end-caps. The use of the beam-spot constraint in the track fit improves the momentum resolution for high-momentum tracks by about 5%. The impact parameter resolutions are quoted only for tracks with a hit in the vertexing layer (this requirement has a very high efficiency, as illustrated in Fig. 14 by the small difference between the standard quality and the b-tagging quality tracks). Figure 7 shows the comparison of the impact parameter resolutions for pions and muons. The muon distributions are very close to Gaussian, while those for the pions are slightly broader and have small tails, in addition. The tails are even larger for electrons, and this is discussed in Section 5.

Track parameter	$0.25 < \eta < 0.50$		$1.50 < \eta < 1.75$	
	$\sigma_X(\infty)$	p_X (GeV)	$\sigma_X(\infty)$	p_X (GeV)
Inverse transverse momentum (q/p_T)	0.34 TeV^{-1}	44	0.41 TeV^{-1}	80
Azimuthal angle (ϕ)	70 rad	39	92 rad	49
Polar angle ($\cot \theta$)	0.7×10^{-3}	5.0	1.2×10^{-3}	10
Transverse impact parameter (d_0)	10 m	14	12 m	20
Longitudinal impact parameter ($z_0 \times \sin \theta$)	91 m	2.3	71 m	3.7

Table 3: Expected track-parameter resolutions (RMS) at infinite transverse momentum, $\sigma_X(\infty)$, and transverse momentum, p_X , at which the multiple-scattering contribution equals that from the detector resolution (see Eq. (1)). The momentum and angular resolutions are shown for muons, whereas the impact-parameter resolutions are shown for pions (see text). The values are shown for two η -regions, one in the barrel inner detector where the amount of material is close to its minimum and one in the end-cap where the amount of material is close to its maximum. Isolated, single particles are used with perfect alignment and calibration in order to indicate the optimal performance.

The consequences of the pseudorapidity variation of the track parameter resolutions can be seen from the reconstructed $J/\psi \rightarrow$ masses in the barrel and end-caps. This is shown in Fig. 8 where both muons are either in the barrel or the end-caps.

The determination of the lepton charge at high p_T is particularly important for measuring charge asymmetries arising from the decays of possible heavy gauge bosons (W' and Z'). Typically, such measurements require that the charge of the particle be determined to better than 3σ ³⁾. Whereas the charge of high-energy muons will be measured precisely in the muon system, the charge of high-energy electrons can only be measured by the inner detector. Figure 9 shows the reconstructed values of q/p_T for negatively charged isolated muons and electrons with $p_T = 0.5 \text{ TeV}$ and $p_T = 2 \text{ TeV}$. The peaks of the distributions are at negative values, reflecting the negative charges of the simulated particles. It can be seen that the shape of the muon distributions is unchanged in going from 0.5 to 2 TeV – at high momentum, the resolution of q/p_T is independent of the true momentum of the muon and determined by the

²⁾Muons suffer less from interactions and hence provide the best reference; impact parameter determination is important for vertexing, and this is more commonly required for hadrons, for example when b -tagging.

³⁾The charge of a particle is considered well measured if it is at least 3σ from 0 in the variable q/p .

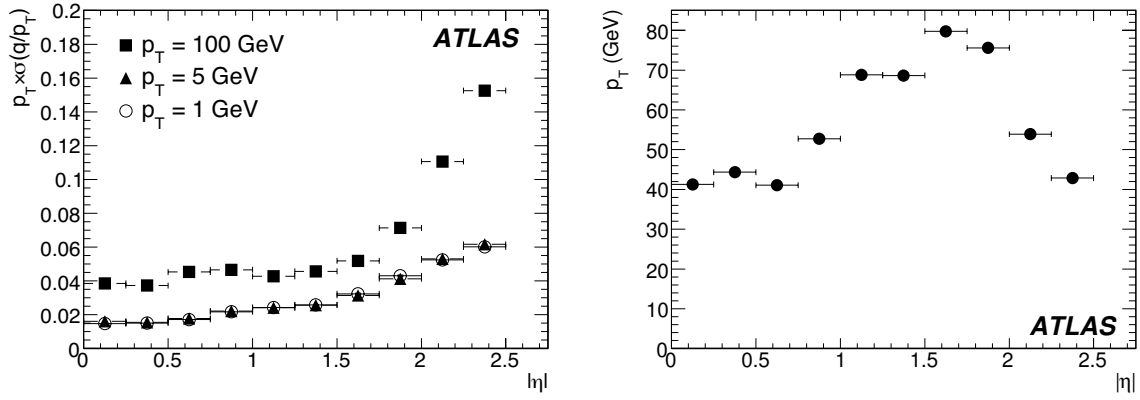


Figure 4: Relative transverse momentum resolution (left) as a function of $|\eta|$ for muons with $p_T = 1, 5$ and 100 GeV. Transverse momentum, at which the multiple-scattering contribution equals the intrinsic resolution (corresponding to p_X in Eq. (1)), as a function of $|\eta|$ (right).

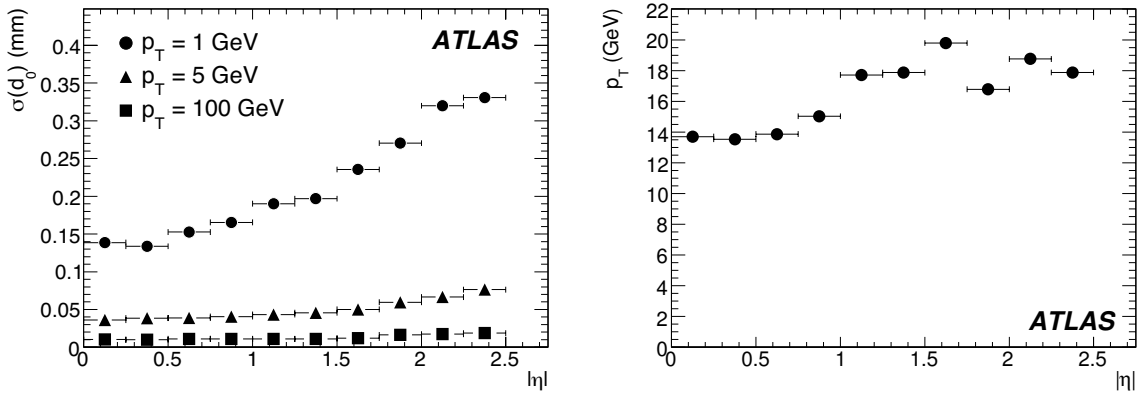


Figure 5: Transverse impact parameter, d_0 , resolution (left) as a function of $|\eta|$ for pions with $p_T = 1, 5$ and 100 GeV. Transverse momentum, at which the multiple-scattering contribution equals the intrinsic resolution (corresponding to p_X in Eq. (1)), as a function of $|\eta|$ (right).

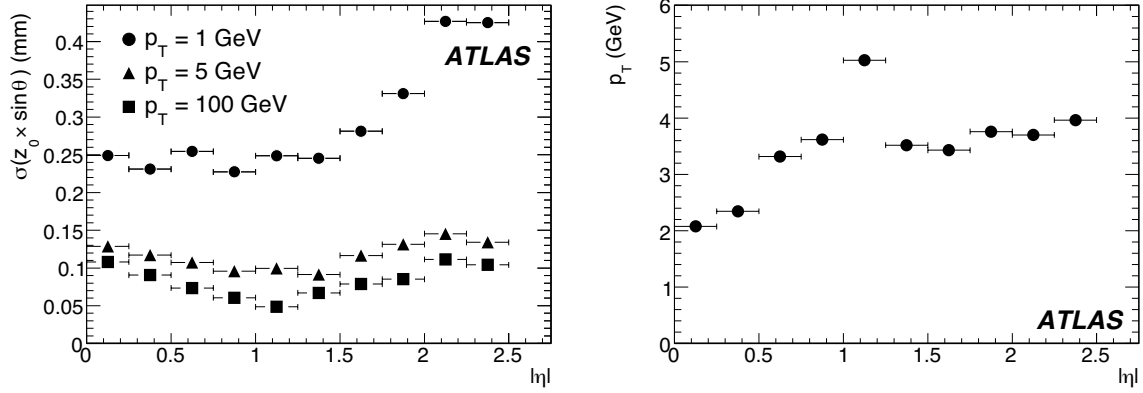


Figure 6: Modified longitudinal impact parameter, $z_0 \times \sin\theta$, resolution (left) as a function of $|\eta|$ for pions with $p_T = 1, 5$ and 100 GeV. Transverse momentum, at which the multiple-scattering contribution equals the intrinsic resolution (corresponding to p_X in Eq. (1)), as a function of $|\eta|$ (right).

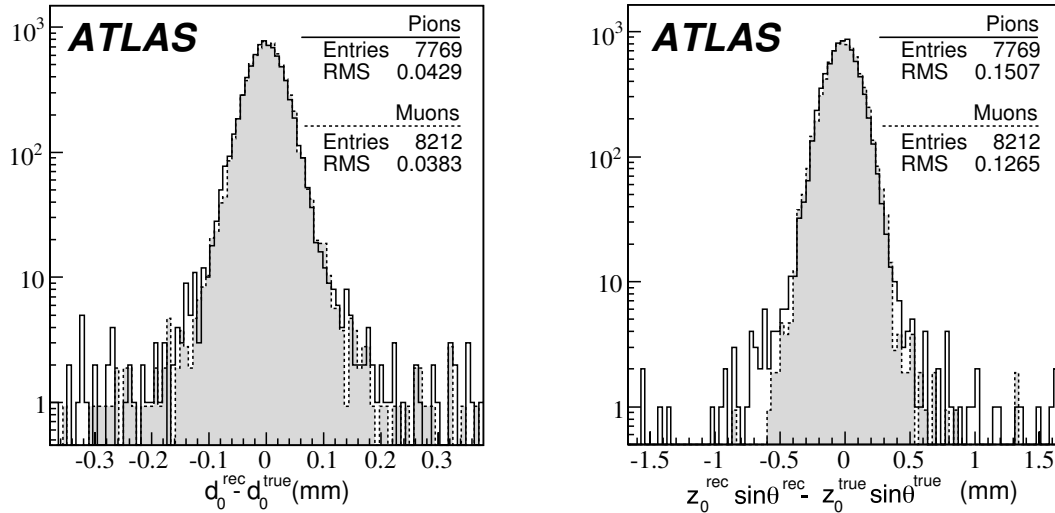


Figure 7: Resolution of the transverse impact parameter, d_0 (left) and the modified longitudinal impact parameter, $z_0 \times \sin\theta$ (right) for 5 GeV muons and pions with $|\eta| \leq 0.5$ – corresponding to the first two bins of the previous two figures.

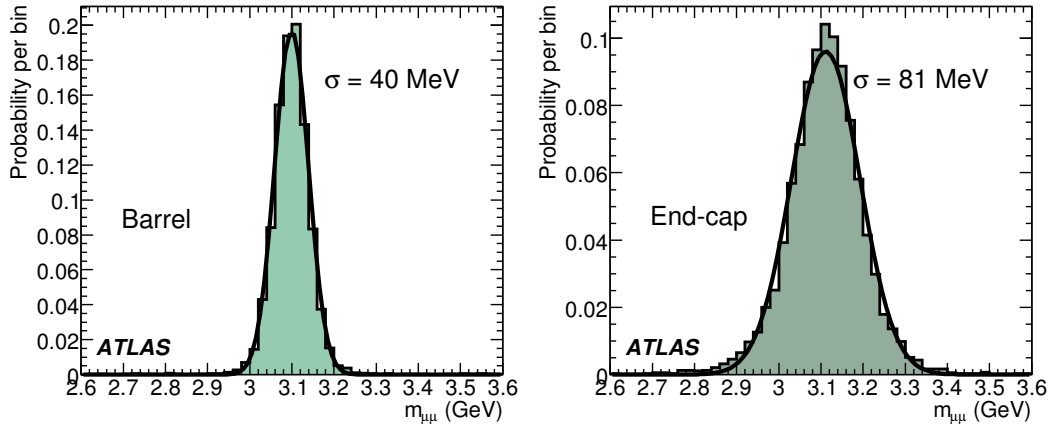


Figure 8: Probability for the reconstructed invariant mass of muon pairs from $J/\psi \rightarrow \mu\mu$ decays in events with prompt J/ψ production. Distributions are shown for both muons with $|\eta| < 0.8$ (left) and $|\eta| > 1.5$ (right).

intrinsic resolution of the detector.

For electrons, things are more complicated. As well as the intrinsic resolution, there are competing effects from bremsstrahlung (which lowers the track momentum and makes the charge easier to measure) and the conversion of bremsstrahlung photons (leading to pattern-recognition problems and degraded charge determination). At 0.5 TeV, the effects of the conversions are significant, causing the electrons to be measured worse than the corresponding muons. However, at 2 TeV, the intrinsic resolution dominates the electron charge misidentification, and this is partially compensated for by the bremsstrahlung. The fractions of muons and electrons for which the sign of the charge is incorrectly determined are shown in Fig. 10. For these plots, perfect alignment has been assumed; any misalignment will degrade the charge sign determination.

3.3 Track reconstruction efficiency

Figures 11, 12 and 13 show the efficiencies for reconstructing isolated muons, pions and electrons. In addition to multiple-scattering, pions are affected by hadronic interactions in the inner detector material, while electrons are subject to even larger reconstruction inefficiencies which arise from the effects of bremsstrahlung. As a result, the efficiency curves as a function of $|\eta|$ for pions and electrons reflect the shape of the amount of material in the inner detector (see Fig. 3). As expected, the efficiency becomes larger and more uniform as a function of $|\eta|$ at higher energies.

Previous studies [1] have shown that the reconstruction efficiency is little affected by the “pile-up” of additional minimum bias events at high luminosity ($10^{34} \text{ cm}^{-2}\text{s}^{-1}$). A more challenging environment is found in the core of an energetic jet. Figure 14 shows the track reconstruction efficiency for prompt pions (produced before the vertexing layer) and the fake rate for tracks in jets in $t\bar{t}$ events as a function of $|\eta|$. For these events, the mean jet p_T is 55 GeV, and the mean p_T of the accepted tracks which they contain is 4 GeV. The loss of efficiency at $|\eta| = 0$ with the b -tagging criteria arises from inefficiencies in the pixel vertexing layer, which are assumed here to be 1%; this improves at higher $|\eta|$, owing to the presence of larger clusters when the track incidence angle decreases. Beyond $|\eta| \sim 1$, the tracking performance deteriorates, mostly because of increased material. As shown in Fig. 15, the fake rate increases near the core of the jet, where the track density is the highest and induces pattern-recognition problems. This

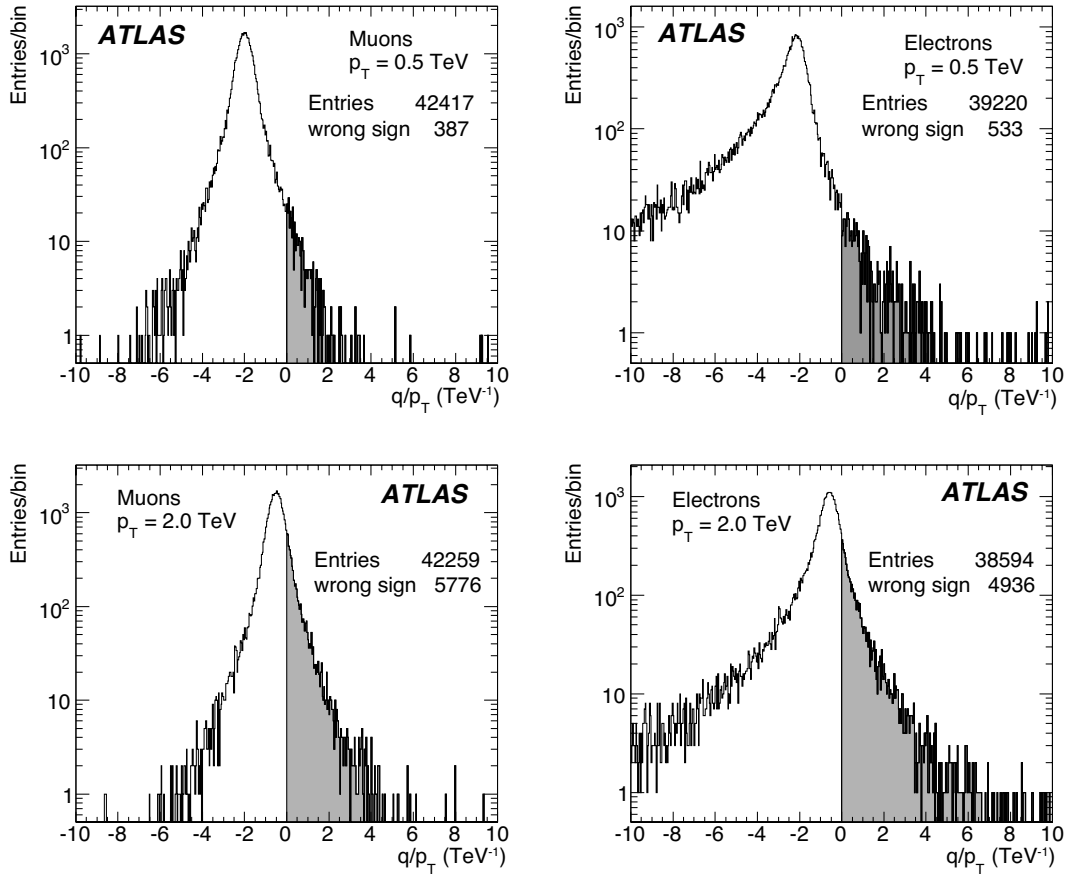


Figure 9: Reconstructed inverse transverse momentum multiplied by the charge for high-energy muons (μ^-) (left) and electrons (e^-) (right) for $p_T = 0.5$ TeV (top) and $p_T = 2$ TeV (bottom) and integrated over a flat distribution in η with $|\eta| \leq 2.5$. Those tracks which have been incorrectly reconstructed with a positive charge are indicated by the shaded regions. At 2 TeV, the fraction of electrons (muons) whose charge has been misidentified is 12.8% (13.7%).

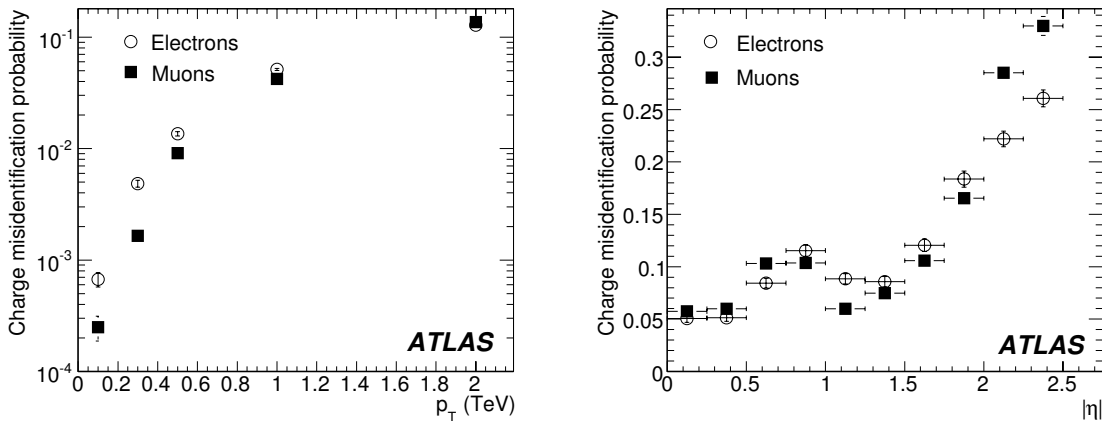


Figure 10: Charge misidentification probability for high-energy muons and electrons as a function of p_T for particles with $|\eta| \leq 2.5$ (left) and as a function of $|\eta|$ for $p_T = 2$ TeV (right).

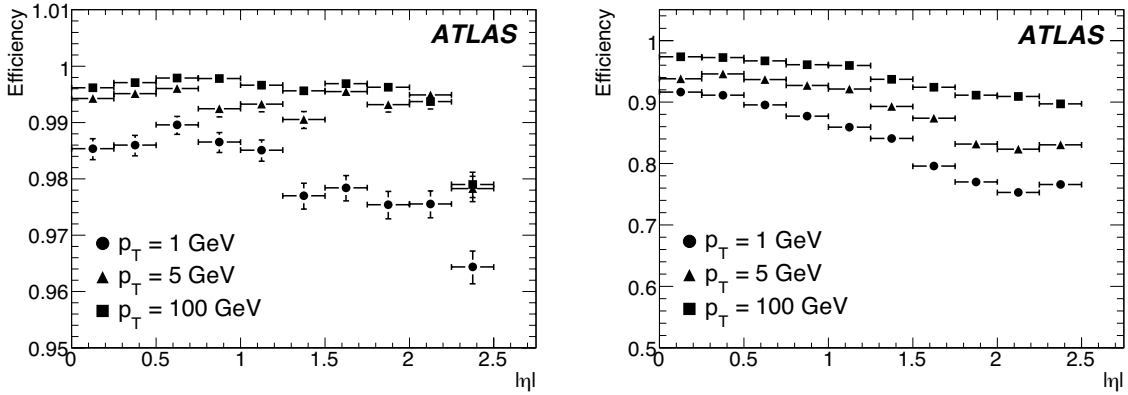


Figure 11: Track reconstruction efficiencies as a function of $|\eta|$ for muons (left) and pions (right) with $p_T = 1, 5$ and 100 GeV.

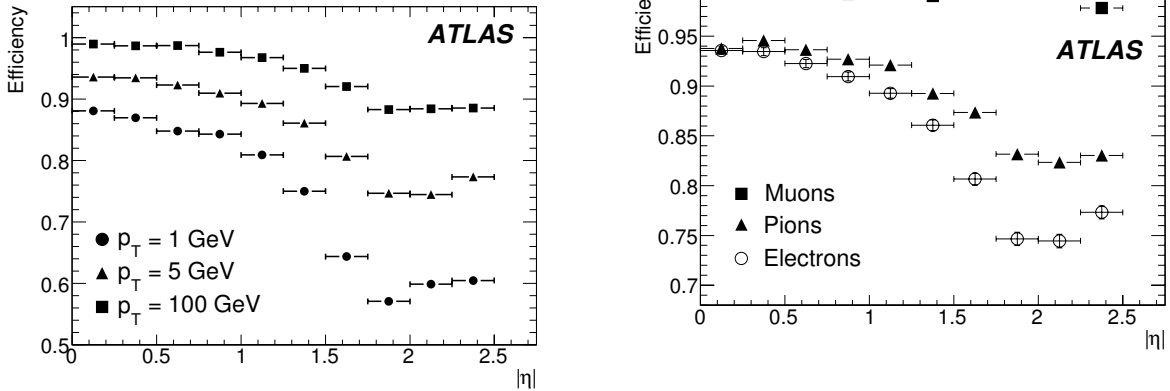


Figure 12: Track reconstruction efficiencies as a function of $|\eta|$ for electrons with $p_T = 1, 5$ and 100 GeV.

Figure 13: Track reconstruction efficiencies as a function of $|\eta|$ for muons, pions and electrons with $p_T = 5$ GeV. The inefficiencies for pions and electrons reflect the shape of the amount of material in the inner detector as a function of $|\eta|$.

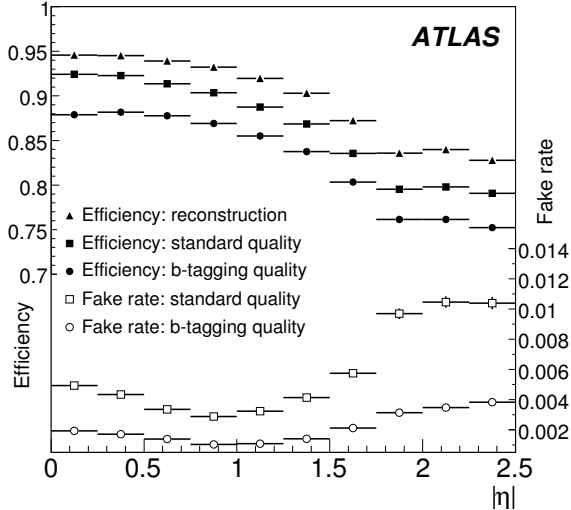


Figure 14: Track reconstruction efficiencies and fake rates as a function of $|\eta|$, for charged pions in jets in $t\bar{t}$ events and for different quality cuts (as described in Section 3.1). “Reconstruction” refers to the basic reconstruction before additional quality cuts.

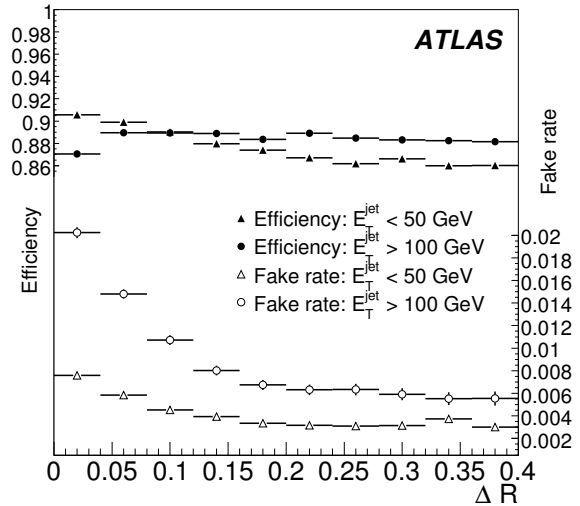


Figure 15: Track reconstruction efficiencies and fake rates as a function of the distance ΔR (defined as $\Delta R = \sqrt{\Delta\eta^2 + \Delta\phi^2}$) of the track to the jet axis, using the standard quality cuts and integrated over $|\eta| < 2.5$, for charged pions in jets in $t\bar{t}$ events.

effect increases as the jet p_T increases. Using alternative algorithms, a few percent efficiency can be gained at the cost of doubling the fake rate in the jet core.

The reconstruction described in Section 2 is aimed at tracks with $p_T > 0.5$ GeV. Multiplicity studies in minimum bias events will be among the first analyses undertaken by ATLAS. In these events, the peak of the track p_T spectrum is around 0.3 GeV. The reconstruction of these low-momentum tracks will be difficult because of the high curvature of the tracks, increased multiple scattering, and at very low momentum, reduced numbers of hits, since the tracks may fail to reach the outer layers of the inner detector. To complement the track-finding strategy described in Section 2, an additional strategy is employed in which hitherto unused pixel and SCT hits are used. To further aid the reconstruction, the algorithm for the space-point track seeding is modified to use looser internal cuts and the cut on the number of precision hits is reduced to at least five hits. Tracks are accepted with $p_T > 0.1$ GeV, and in some cases, inefficiencies for $p_T > 0.5$ GeV are recovered. The resulting track reconstruction efficiency is shown in Fig. 16. The distribution of candidate fake tracks is shown in Fig. 17.

4 Vertexing performance

4.1 Primary vertices

Vertexing tools constitute important components of the higher-level tracking algorithms. The residuals of the primary vertex reconstruction are shown in Fig. 18, as obtained without using any beam constraint, for $t\bar{t}$ events and $H \rightarrow \gamma\gamma$ events with $m_H = 120$ GeV. The results shown here for $H \rightarrow \gamma\gamma$ events are based on tracks reconstructed from the underlying event and do not make use of the measurement of the photon direction in the electromagnetic calorimeter. The primary vertex in $t\bar{t}$ events has always a rather large multiplicity and includes a number of high- p_T tracks, resulting in a narrower and more Gaussian distribution than for $H \rightarrow \gamma\gamma$ events. Table 4 shows the resolutions of the primary vertex reconstruction

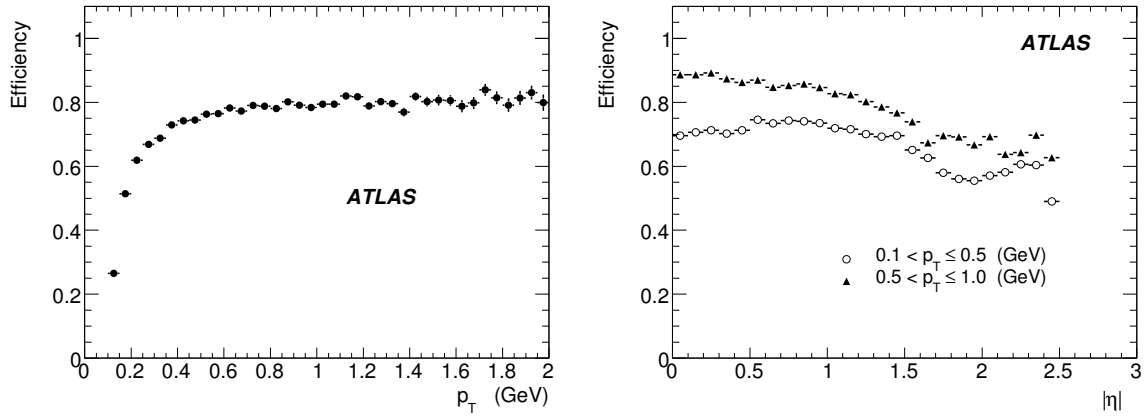


Figure 16: Track reconstruction efficiencies as a function of p_T for $|\eta| < 2.5$ and $p_T > 0.1$ GeV (left) and as a function of $|\eta|$ for two different p_T ranges (right) in minimum bias events (non-diffractive inelastic events).

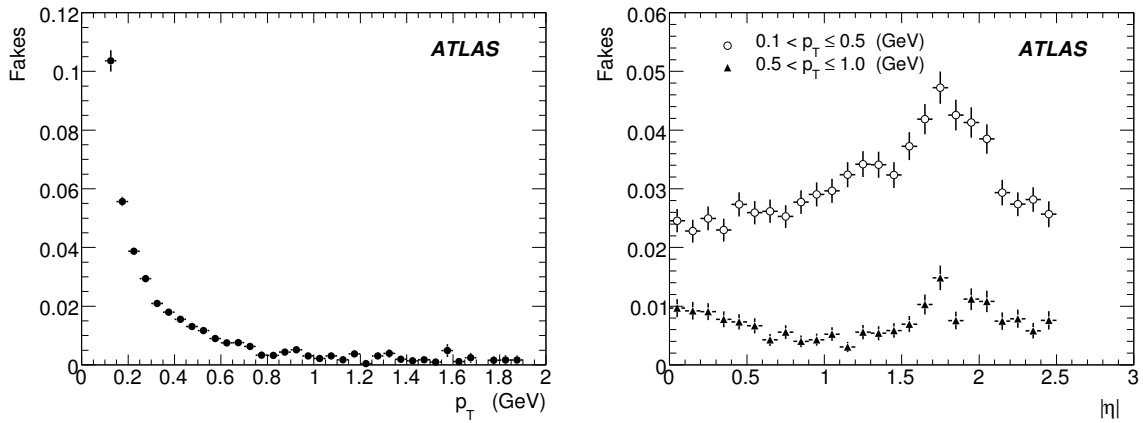


Figure 17: Rate of candidate fake tracks as a function of p_T for $|\eta| < 2.5$ and $p_T > 0.1$ GeV (left) and as a function of $|\eta|$ (right) in minimum bias events (non-diffractive inelastic events). The rate of such tracks is a function of the amount of material, indicating that a large fraction of them are secondaries for which the Monte-Carlo truth information is not kept

in these $t\bar{t}$ and $H \rightarrow \gamma\gamma$ events, without and with a beam constraint in the transverse plane, as well as the efficiencies to reconstruct and select correctly (within ± 300 m) these primary vertices in the presence of pile-up at a luminosity of $10^{33} \text{ cm}^{-2}\text{s}^{-1}$.

Event type	x-y resolution (m)	z resolution (m)	Reconstruction efficiency (%)	Selection efficiency (%)
$t\bar{t}$ (no BC)	18	41	100	99
$t\bar{t}$ (BC)	11	40	100	99
$H \rightarrow \gamma\gamma$ (no BC)	36	72	96	79
$H \rightarrow \gamma\gamma$ (BC)	14	66	96	79

Table 4: Primary vertex resolutions (RMS), without and with a beam constraint (BC) in the transverse plane, for $t\bar{t}$ events and $H \rightarrow \gamma\gamma$ events with $m_H = 120$ GeV in the absence of pile-up. Also shown, in the presence of pile-up at a luminosity of $10^{33} \text{ cm}^{-2}\text{s}^{-1}$, are the efficiencies to reconstruct and then select the hard-scattering vertex within ± 300 m of the true vertex position in z . The hard-scattering vertex is selected as the primary vertex with the largest Σp_T^2 , summed over all its constituent tracks.

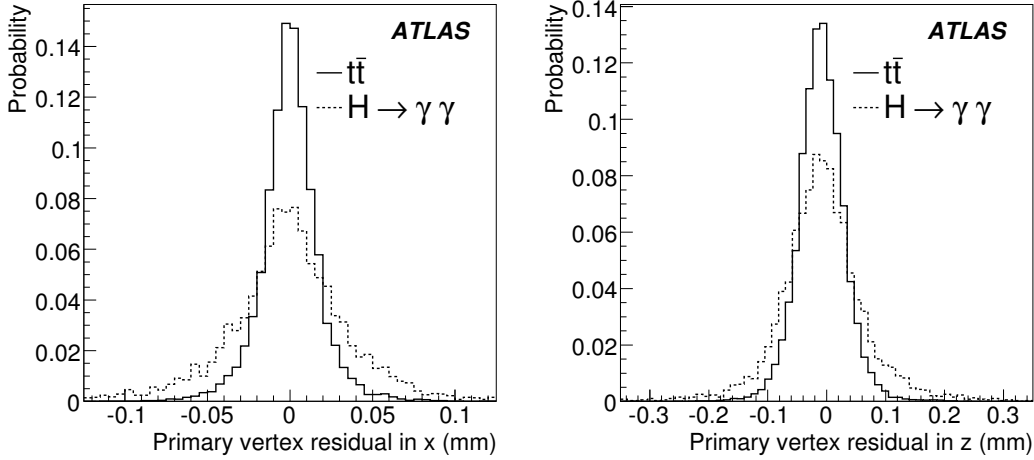


Figure 18: Primary vertex residual along x , in the transverse plane (left), and along z , parallel to the beam (right), for events containing top-quark pairs and $H \rightarrow \gamma\gamma$ decays with $m_H = 120$ GeV. The results are shown without pile-up and without any beam constraint.

4.2 Secondary vertices

The resolution for the reconstruction of the radial position of secondary vertices for $J/\psi \rightarrow$ decays in events containing B -hadron decays (mean p_T of 15 GeV for the J/ψ) is shown in Fig. 19. While there are some tails in the resolution distributions (left-hand plot), these are small. The corresponding distributions for three-prong hadronic τ -decays in $Z \rightarrow \tau\tau$ events (mean p_T of 36 GeV for the τ -lepton) are shown in Fig. 20. Because there are three charged tracks in close proximity, the reconstruction of these decays is more challenging: the vertex resolutions are Gaussian in the central region, but have long tails as can be seen from the points showing 95% coverage in right-hand plot.

Finally, Fig. 21 shows the resolution as a function of decay radius for the reconstruction of the radial

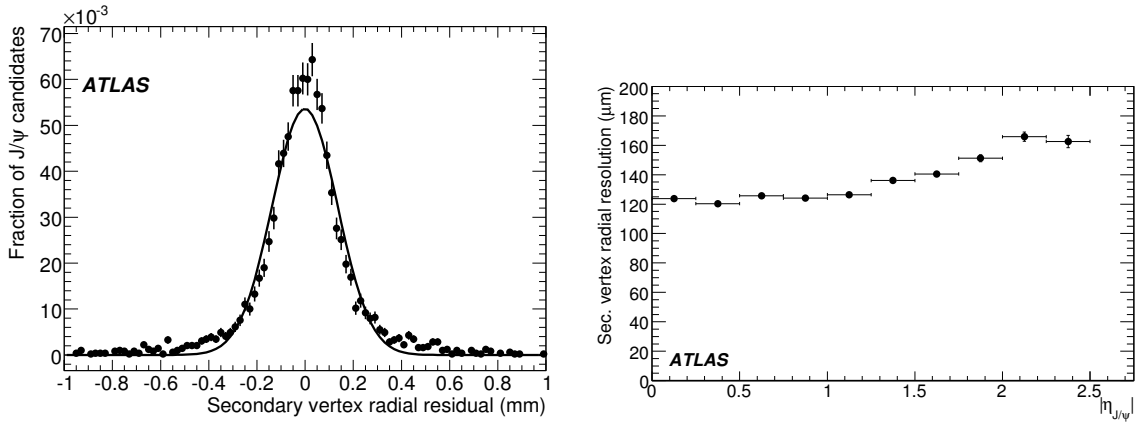


Figure 19: Resolution for the reconstruction of the radial position of the secondary vertex for $J/\psi \rightarrow$ decays in events containing B -hadron decays for tracks with $|\eta|$ around 0 (left) and as a function of the pseudorapidity of the J/ψ (right). The J/ψ have an average transverse momentum of 15 GeV.

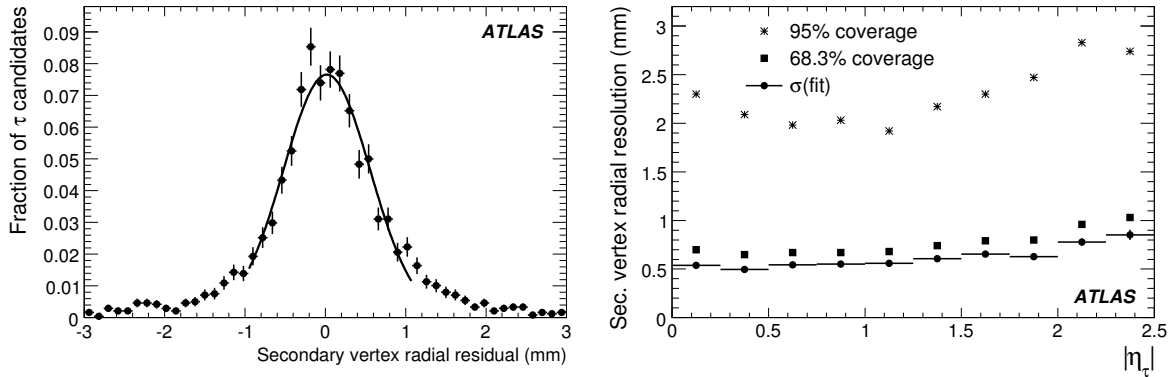


Figure 20: Resolution for the reconstruction of the radial position of the secondary vertex for three-prong hadronic τ -decays in $Z \rightarrow \tau\tau$ events for tracks with $|\eta|$ around 0 (left) and as a function of the pseudorapidity of the τ (right). In the right-hand plot, the circles with bars correspond to Gaussian fits, as illustrated in the left-hand plot; the points showing 68.3% (95%) coverage show the width of the integrated distribution containing 68.3% (95%) of the measurements (corresponding to 1σ (2σ) for a Gaussian distribution). The τ -leptons have an average transverse momentum of 36 GeV.

position of secondary vertices for K_s^0 decays (mean p_T of 6 GeV) in events containing B -hadron decays. The resolution in each radial slice is determined from a Gaussian fit to the core of the distribution. It can be seen that there are significant tails: just before the barrel layers, the resolution for decays in the barrel region is good, giving rise to the core; while that from the end-caps is variable, depending on the actual position of the decay, giving rise to a broader distribution. The tails can be reduced and the resolutions improved somewhat by tighter cuts on track quality and the reconstructed invariant mass, if desirable. The effect of crossing the three successive pixel layers is clearly visible as well as the degraded resolution for decays beyond the last pixel layer. Figure 22 shows the resolution as a function of decay radius for the reconstruction of the invariant mass of the charged-pion pair for the same $K_s^0 \rightarrow \pi^+ \pi^-$ decays. Figure 23 shows the efficiency to reconstruct the K_s^0 decays. The reconstruction requires 3D information provided by the silicon detectors, and hence the efficiency falls to zero once the decay is beyond the penultimate SCT layers.

5 Particle identification, reconstruction of electrons and photon conversions

The reconstruction of electrons and of photon conversions is a particular challenge for the inner detector. The fraction of energy lost by electrons traversing the inner detector is shown in Fig. 24. In the energy range over which the inner detector will measure electrons, the fraction has little dependence on the actual electron energy. Electrons lose on average between 20 to 50% of their energy (depending on $|\eta|$) by the time they have left the SCT, as illustrated in Fig. 25. The probability for photons to convert is fairly independent of their energies for $p_T > 1$ GeV. A histogram of the location of photon conversions in $|\eta| < 0.8$ is shown in Fig. 26 - the radial structure of the detector is clearly visible. Between 10 to 50% of photons have converted into an electron-positron pair before leaving the SCT, as illustrated in Fig. 27.

The TRT plays a central role in electron identification, cross-checking and complementing the electromagnetic calorimeter, especially at energies below 25 GeV [2]. In addition, the TRT contributes to the reconstruction and identification of electron track segments from photon conversions down to 1 GeV and of electrons which have radiated a large fraction of their energy in the silicon layers.

5.1 Electron reconstruction

In the absence of bremsstrahlung, the distribution p_{true}/p_{recon} should be Gaussian; but in the presence of bremsstrahlung, this is far from true, as can be seen for the end-cap in Fig. 28 (left-hand plot). By fitting electron tracks in such a way as to allow for bremsstrahlung, it is possible to improve the reconstructed track parameters, as shown in Figs. 28 and 29 for two examples of bremsstrahlung recovery algorithms. These algorithms rely exclusively on the inner detector information and therefore provide significant improvements only for electron energies below ~ 25 GeV. The dynamic noise adjustment (DNA) method extrapolates track segments to the next silicon detector layer. If there is a significant χ^2 contribution, compatible with a hard bremsstrahlung, the energy loss is estimated and an additional noise term is included in the Kalman filter [9]. The Gaussian-sum filter (GSF) is a non-linear generalisation of the Kalman filter, which takes into account non-Gaussian noise by modelling it as a weighted sum of Gaussian components and therefore acts as a weighted sum of Kalman filters operating in parallel [10]. With real data, to improve the fitted track parameters for electrons without deteriorating the fits for non-electrons, it is necessary to assess whether a track is likely to correspond to an electron or not. This can be done to some extent by the algorithms themselves by looking at the fits; additional information can be obtained from the transition radiation in the TRT (see 5.2) and the electromagnetic calorimeter. Ultimately, since information is lost during the bremsstrahlung, there is an unavoidable degradation of

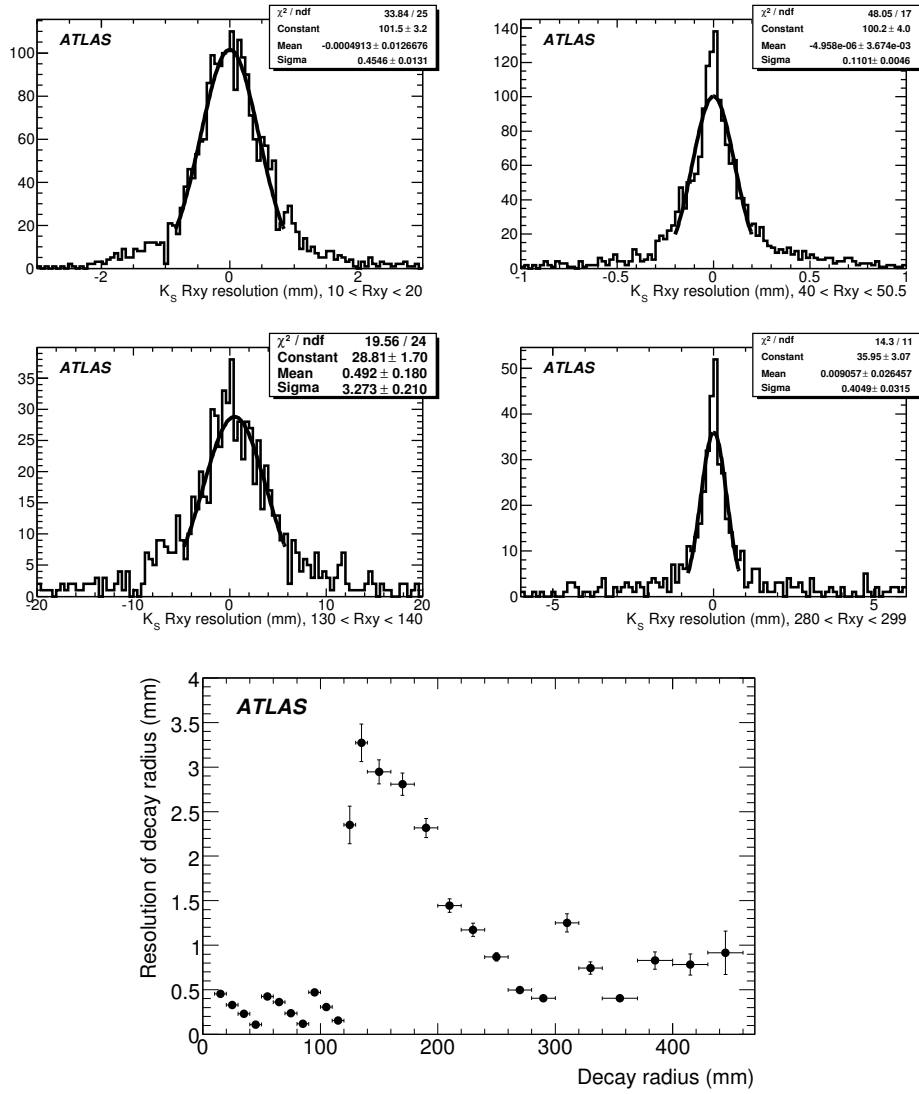


Figure 21: Resolution for the reconstructed radial position of the secondary vertex for $K_s^0 \rightarrow \pi^+\pi^-$ decays in events containing B -hadron decays in various radial intervals (upper) and as a function of the K_s^0 decay radius (lower). The resolutions are best for decays just in front of the detector layers. The barrel pixel layers are at: 51, 89 and 123 mm; the first two SCT layers are at 299 and 371 mm.

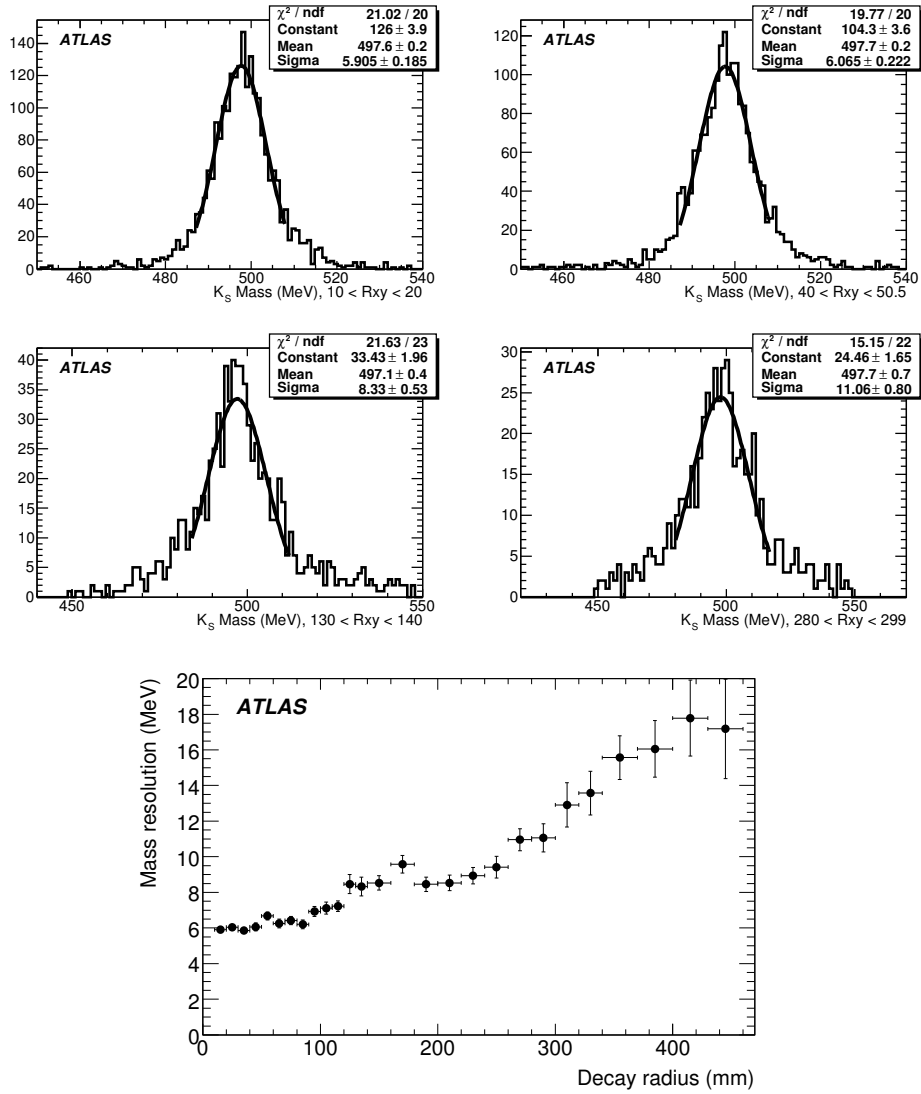


Figure 22: Resolution for the reconstruction of the invariant mass of the charged-pion pair for $K_s^0 \rightarrow \pi^+ \pi^-$ decays in events containing B -hadron decays in various radial intervals (upper) and as a function of the K_s^0 decay radius (lower).

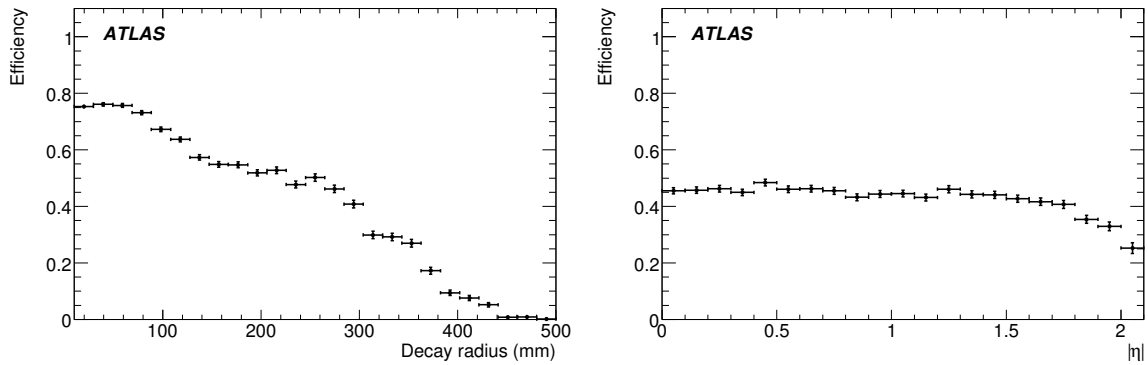


Figure 23: Efficiency to reconstruct charged-pion pairs for $K_s^0 \rightarrow \pi^+\pi^-$ decays in events containing B -hadron decays as a function of the K_s^0 decay radius (left) and as a function of the $|\eta|$ of the K_s^0 (right).

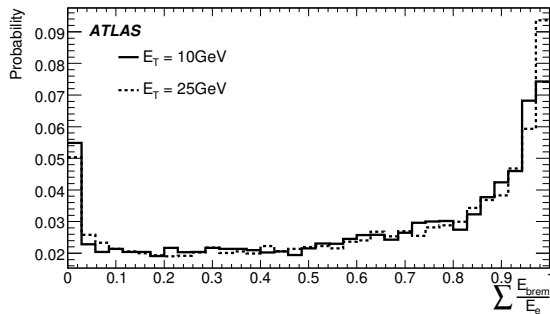


Figure 24: Probability distribution as a function of the fraction of energy lost by electrons with $p_T = 10$ GeV and 25 GeV (integrated over a flat distribution in η with $|\eta| \leq 2.5$) traversing the complete inner detector.

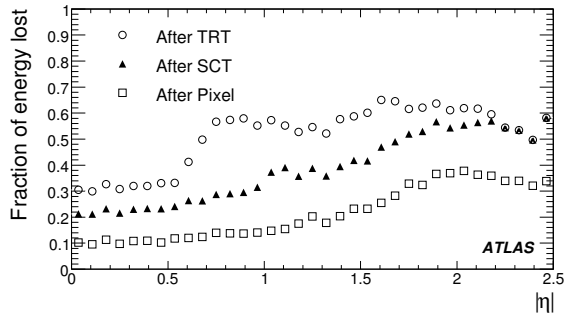


Figure 25: Fraction of energy lost on average by electrons with $p_T = 25$ GeV as a function of $|\eta|$, when exiting the pixel, the SCT and the inner detector tracking volumes. For $|\eta| > 2.2$, there is no TRT material, hence the SCT and TRT lines merge.

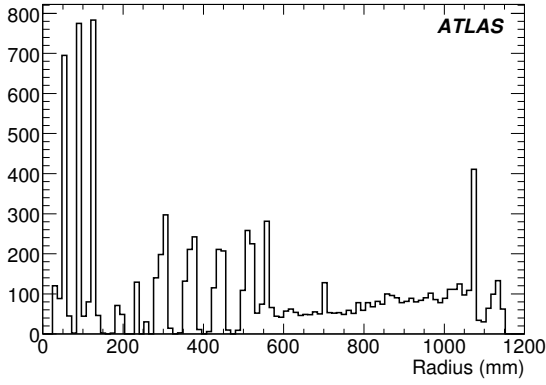


Figure 26: Radial position of photon conversions in the barrel region ($|\eta| < 0.8$) deduced from Monte-Carlo truth information (arbitrary normalisation).

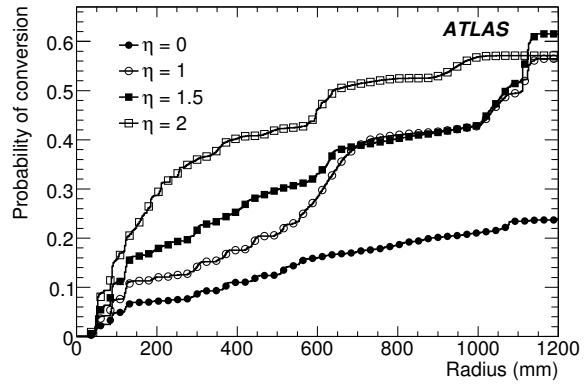


Figure 27: Probability for a photon to have converted as a function of radius for different values of $|\eta|$, shown for photons with $p_T > 1$ GeV in minimum bias events.

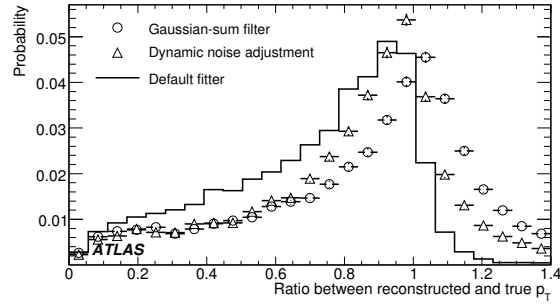
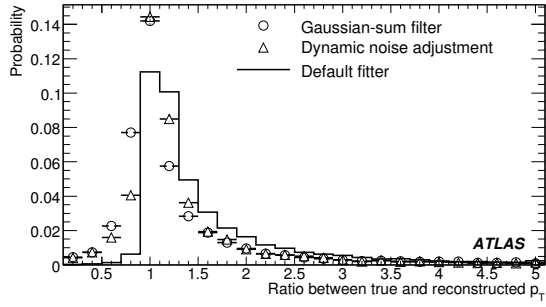


Figure 28: Probability distributions for the ratio of the true to reconstructed momentum (left) and its reciprocal (right) for electrons with $p_T = 25$ GeV and $|\eta| > 1.5$. The results are shown as probabilities per bin for the default Kalman fitter and for two bremsstrahlung recovery algorithms (see text).

the electron measurement. The algorithms serve to reduce the bias of the track fits caused by the increased track curvature. Only by adding additional information, such as the position of the cluster in the electromagnetic calorimeter [2], is it possible to make a real improvement on the measured momentum.

By allowing for changes in the curvature of the track, the bremsstrahlung recovery algorithms “follow” the tracks better and correctly associate more of the hits, leading to improvements in the reconstruction efficiencies, as can be seen in Fig. 30. GSF has 2-3% greater efficiency than the default reconstruction, since it does not flag hits as outliers, hence a track is less likely to fail the quality cuts on the numbers of hits.

Figure 31 shows the improvements from bremsstrahlung recovery for the reconstructed $J/\psi \rightarrow ee$ mass. Integrating over the complete pseudorapidity acceptance of the ID, and without using any bremsstrahlung recovery, only 42% of events are reconstructed within ± 500 MeV of the nominal J/ψ mass, whereas with the use of the bremsstrahlung recovery, this fraction increases to 53% and 56% for DNA and GSF respectively, and the bias of the peak position is reduced. In the inner detector alone, the J/ψ signal in the end-caps is more or less completely lost because of the effects of the increased material compared to that in the barrel. The poor performance in the end-caps arises from the significant fraction of energy lost by electrons (O(30)% by the time they have left the pixels) as well as the change in track

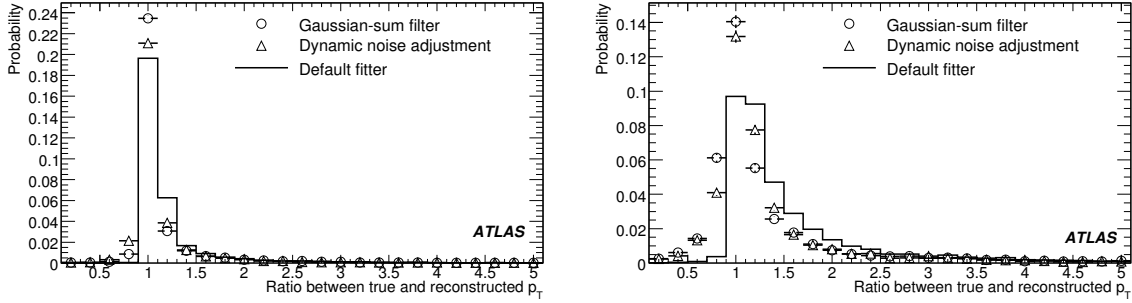


Figure 29: Probability distributions for the ratio of the true to reconstructed momentum for electrons with $p_T = 25$ GeV and $|\eta| < 0.8$ (left) and $p_T = 10$ GeV and $|\eta| > 1.5$ (right). The results are shown as probabilities per bin for the default Kalman fitter and for two bremsstrahlung recovery algorithms (see text).

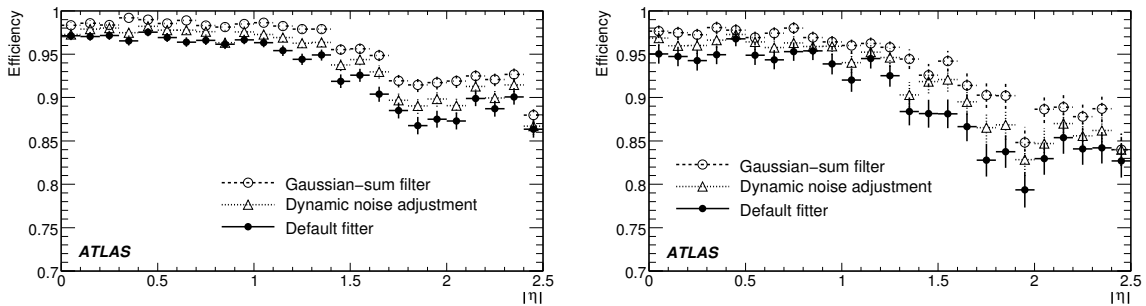


Figure 30: Efficiencies to reconstruct electrons as a function of $|\eta|$ for electrons with $p_T = 25$ GeV (left) and $p_T = 10$ GeV (right). The results are shown for the default Kalman fitter and for two bremsstrahlung recovery algorithms (see text).

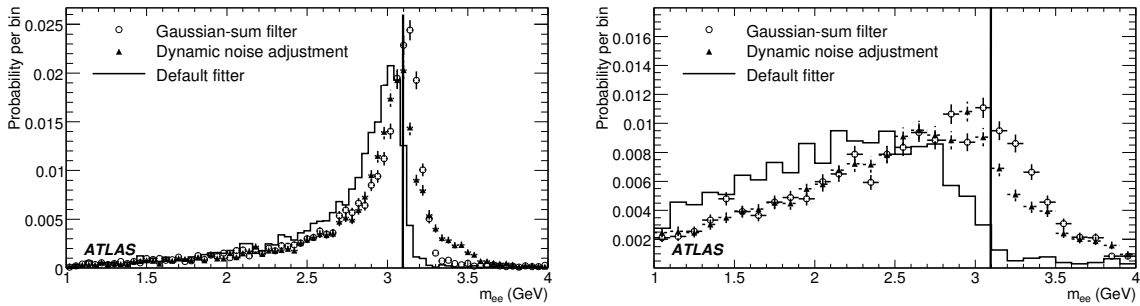


Figure 31: Probability for the reconstructed invariant mass of electron pairs from $J/\psi \rightarrow ee$ decays in events with $B_d^0 \rightarrow J/\psi(ee)K_s^0$. Distributions are shown for both electrons with $|\eta| < 0.8$ (left) and $|\eta| > 1.5$ (right). The results are shown for the default Kalman fitter and for two bremsstrahlung recovery algorithms (see text). The true J/ψ mass is shown by the vertical line.

direction. These distributions should be contrasted with those for the muonic decays of the J/ψ in Fig. 8.

To conclude, the material of the inner detector causes a significant amount of bremsstrahlung for electrons, biasing their fitted parameters. This can be partially compensated within the inner detector using the so-called bremsstrahlung recovery procedures, DNA and GSF. These algorithms should be applied to tracks in a way so as to improve electrons and not degrade pions or muons. DNA runs in a time comparable with other simple fitters, while GSF, albeit producing better results, is a factor of twenty slower than DNA. Exactly how these algorithms are used will depend on individual physics analyses.

5.2 Electron identification

While the end-cap TRT (discrete radiator foils) is relatively easy to simulate, the barrel TRT (matrix of fibres) is harder and the best indication of the expected performance comes from the test beam (CTB), where a complete barrel TRT module was tested. Using pion, electron and muon samples in the energy range between 2 and 350 GeV, the barrel TRT response has been measured in the CTB in terms of the high-threshold hit probability, as shown in Fig. 32. The measured performance has been used to parametrise the response in the TRT barrel. The transition-radiation X-rays contribute significantly to the high-threshold hits for electron energies above 2 GeV and saturation sets in for electron energies above 10 GeV. Figure 33 shows the resulting pion identification efficiency (probability of pions being misidentified as electrons) for an electron efficiency of 90%, achieved by performing a likelihood evaluation based on the high-threshold probability for electrons and pions for each straw. Figure 33 also shows the effect of including time-over-threshold information, which improves the pion rejection by about a factor of two when combined with the high-threshold hit information. At low energies, the pion rejection (the inverse of the pion efficiency plotted in Fig. 33) improves with energy as the electrons emit more transition radiation. The performance is optimal at energies of ~ 5 GeV, and pion-rejection factors above 50 are achieved in the energy range of 2–20 GeV. At very high energies, the pions become relativistic and therefore produce more δ -rays and eventually emit transition radiation, which explains why the rejection slowly decreases for energies above 10 GeV.

The electron-identification performance expected for the TRT in ATLAS, including the time-over-threshold information, is shown as a function of $|\eta|$ in Fig. 35 in the form of the pion identification efficiency expected for an electron efficiency of 90% or 95%. The shape observed is closely correlated to the number of TRT straws crossed by the track (see Fig. 34), which decreases from approximately 35 to a minimum of 20 in the transition region between the barrel and end-cap TRT, $0.8 < |\eta| < 1.1$, and which

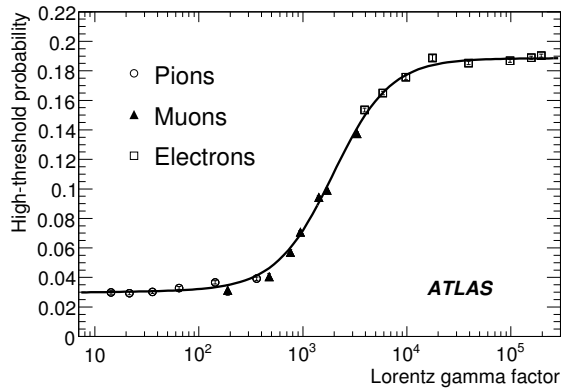


Figure 32: Average probability of a high-threshold hit in the barrel TRT as a function of the Lorentz γ -factor for electrons (open squares), muons (full triangles) and pions (open circles) in the energy range 2–350 GeV, as measured in the combined test-beam (CTB).

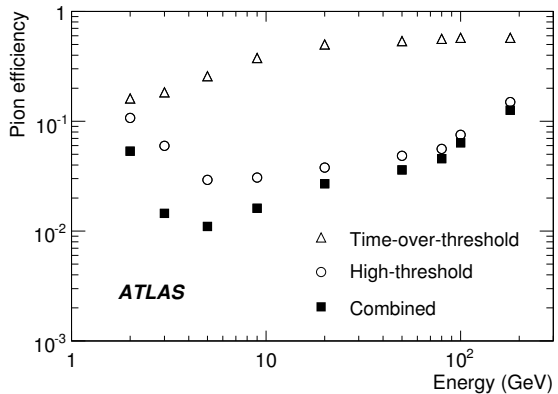


Figure 33: Pion efficiency shown as a function of the pion energy for 90% electron efficiency, using high-threshold hits (open circles), time-over-threshold (open triangles) and their combination (full squares), as measured in the combined test-beam.

also decreases rapidly at the edge of the TRT fiducial acceptance for $|\eta| > 1.8$. Because of its more efficient and regular foil radiator, the performance in the end-cap TRT is better than in the barrel TRT where it consists of radiating fibres [2].

5.3 Conversion reconstruction

Figure 36 shows the efficiency for reconstructing conversions of photons with $p_T = 20$ GeV and $|\eta| < 2.1$ as a function of the conversion radius and pseudorapidity, using the standard tracking algorithm combined with the back-tracking algorithm described in Section 2. At radii above 50 cm, the efficiency for reconstructing single tracks drops and that for reconstructing the pair drops even faster because the two tracks are merged. If both tracks from the photon conversion are reconstructed successfully, vertexing tools can be used to reconstruct the photon conversion with high efficiency up to radii of 50 cm. The overall conversion-identification efficiency can be greatly increased at large radii by flagging single tracks as photon conversions under certain conditions. (The identification is distinct from the reconstruction, since with a single electron, the photon conversion cannot be reconstructed.) Only tracks which have no hits in the vertexing layer, which are not associated to any fitted primary or secondary vertex, and which pass a loose electron identification cut requiring more than 9% high-threshold hits on the TRT segment of the track are retained. The resulting overall efficiency for identifying photon conversions is almost uniform over all radii below 80 cm, as shown in Fig. 37.

6 Conclusions

This paper documents the expected performance for the ATLAS inner detector, focusing on the low-luminosity running at the start-up of the LHC. Most of the performance specifications set out in [1] have been met – it is only at larger values of $|\eta|$, where there are significant amounts of material, that the track-finding efficiencies are less than the targets.

The reconstruction of muons, electrons and pions has been studied in detail as a function of transverse momentum and pseudorapidity. For high- p_T muons in the barrel region, the resolution for $1/p_T$ is

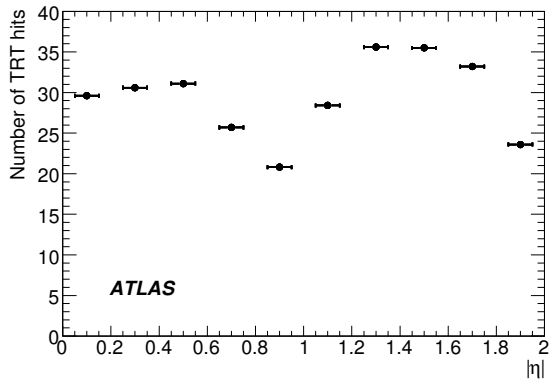


Figure 34: Number of hits on a track as a function of $|\eta|$ for a track crossing the TRT.

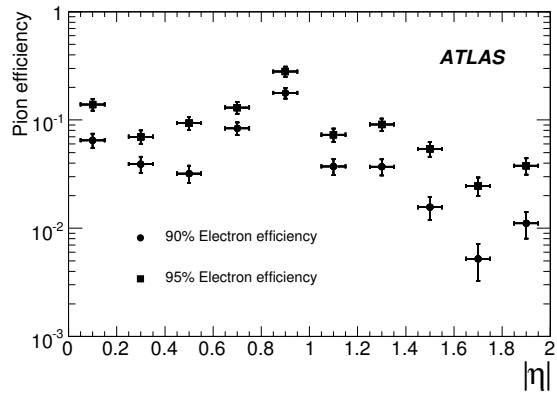


Figure 35: Pion efficiency expected from simulation as a function of $|\eta|$ for an efficiency of 90% or 95% for electrons with $p_T = 25$ GeV.

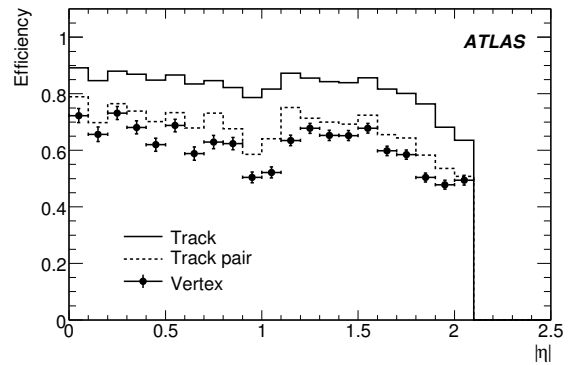
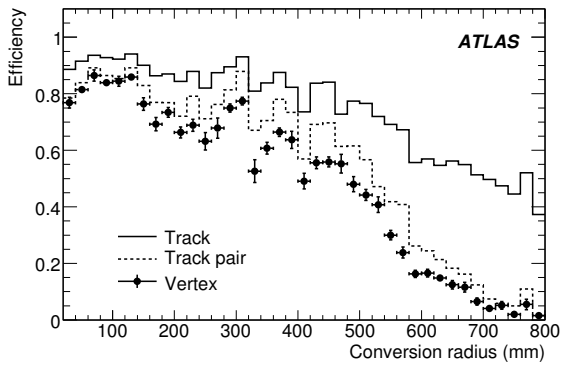


Figure 36: Efficiency to reconstruct conversions of photons with $p_T = 20$ GeV and $|\eta| < 2.1$, as a function of the conversion radius (left) and pseudorapidity (right). Shown are the efficiencies to reconstruct single tracks from conversions, the pair of tracks from the conversion and the conversion vertex.

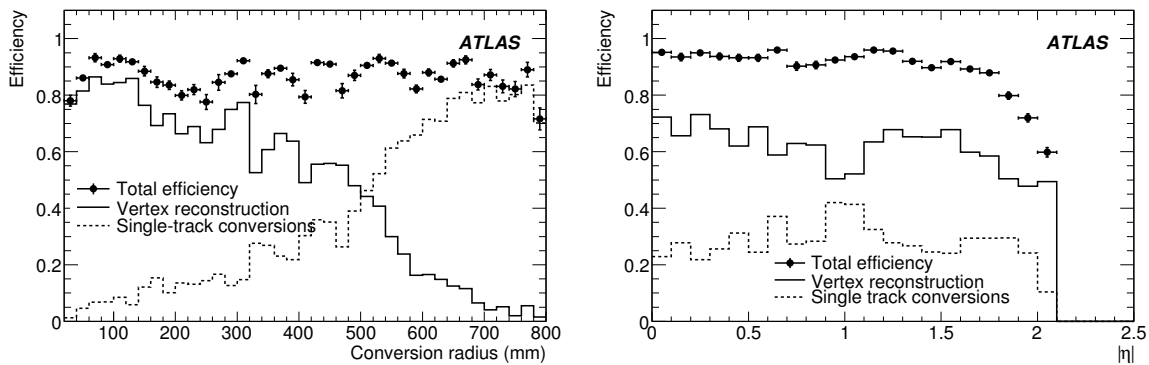


Figure 37: Efficiency to identify conversions of photons with $p_T = 20$ GeV and $|\eta| < 2.1$, as a function of the conversion radius (left) and pseudorapidity (right). The overall efficiency is a combination of the efficiency to reconstruct the conversion vertex, as shown also in Fig. 36, and of that to identify single-track conversions (see text).

expected to be 0.34 TeV^{-1} and the resolution for the transverse impact parameter $10 \text{ } \mu\text{m}$. The charge of muons and electrons will be measured in the inner detector over the complete acceptance up to 1 TeV with misidentification probabilities on average of no more than a few percent. In the barrel region, muons with $p_T \geq 1$ GeV can be identified with efficiencies in excess of 98%. For high- p_T muons, this rises to $\geq 99.5\%$ across the whole acceptance. Electrons and pions suffer from material effects; for tracks around 5 GeV, they are reconstructed with efficiencies between 70 and 95%. The inner detector is able to reconstruct pions down to 0.2 GeV with efficiencies around 50%. Fake rates are low; even in the core of moderate-energy jets ($O(50) \text{ GeV } E_T$), rates are less than 1%.

Algorithms have been developed to reconstruct primary and secondary vertices, as well as K_s^0 (and other V^0 s) decays and conversions. In the case of $t\bar{t}$ events, primary vertices can be identified with 99% efficiency in the presence of low-luminosity pile-up. K_s^0 decays can be reconstructed up to a radius of 400 mm, while conversions can be identified by reconstructing pairs of tracks or tagging single electrons in the TRT with 80% efficiency all the way up to a radius of 800 mm.

Electrons suffer from bremsstrahlung caused by the significant material in the inner detector. Algorithms have been developed to improve the reconstruction of electrons, reducing the bias on the measured momentum. While reasonable electron reconstruction is possible in the inner detector barrel, it is quite difficult in the end-caps because of the increased amount of bremsstrahlung – here, the use of the electromagnetic calorimeter will be essential. Electrons can be identified by their transition radiation in the TRT. For an electron efficiency of 90% at $p_T = 25$ GeV, the pion misidentification probability is of the order of a few percent over most of the acceptance, and the pion rejection will be optimal around 5 GeV.

After many years of preparing the ATLAS inner detector software and having tested it on simulated and test-beam data, we are ready to reconstruct and analyse data from collisions. We now look forward to the first data from the LHC.

References

- [1] The ATLAS Collaboration, Inner Detector: Technical Design Report, CERN/LHCC/97-016/017 (1997).

- [2] The ATLAS Collaboration, G. Aad et al., The ATLAS Experiment at the CERN Large Hardon Collider, 2008 JINST **3** S08003.
- [3] S. Gonzalez-Sevilla et al., Alignment of the pixel and SCT modules for the 2004 ATLAS combined test-beam, ATLAS Note ATL-INDET-PUB-2007-014 (2007).
- [4] E. Abat et al., Combined performance tests before installation of the ATLAS Semiconductor and Transition Radiation Tracking Detectors, JINST **3** (2008) P08003.
- [5] T. Cornelissen et al., Concepts, Design and Implementation of the ATLAS New Tracking, ATLAS Note ATL-SOFT-PUB-2007-007 (2007).
- [6] P.F. Akesson et al., ATLAS Tracking Event Data Model, ATLAS Note ATL-SOFT-PUB-2006-004 (2006); T. G. Cornelissen et al., Updates of the ATLAS Tracking Event Data Model, ATLAS Note ATL-SOFT-PUB-2007-003 (2007).
- [7] A. Salzburger, S. Todorova and M. Wolter, The ATLAS Tracking Geometry Description, ATLAS Note ATL-SOFT-PUB-2007-004 (2007).
- [8] A. Salzburger, The ATLAS Track Extrapolation Package, ATLAS Note ATL-SOFT-PUB-2007-005 (2007).
- [9] V. Kartvelishvili, Nucl. Phys. B (Proc. Suppl.) **172** (2007) 208–211.
- [10] R. Frühwirth, Comp. Phys. Comm. **100** (1997) 1.
- [11] R. Frühwirth and A. Strandlie, Comp. Phys. Comm. **120** (1999) 197–214.
- [12] The ATLAS Collaboration, xKalman and iPatRec, ATLAS Inner Detector Technical Design Report, CERN/LHCC/97-16 (1997) 37-40.
- [13] T. Cornelissen et al., Single Track Performance of the Inner Detector New Track Reconstruction (NEWT), ATLAS Note ATL-INDET-PUB-2008-002 (2008).